Space-based Sub-THz ISAR for space situational awareness – concept and design

Marchetti, Emidio; Stove, Andrew; Hoare, Edward; Cherniakov, Mike; Blacknell , David; Gashinova, Marina

DOI:
10.1109/TAES.2021.3126375

Space-based Sub-THz ISAR for Space Situational Awareness – Concept and Design

Emidio Marchetti, Andrew G. Stove, *SMIEEE*, Edward G. Hoare, *SMIEEE*, Mikhail Cherniakov, David Blacknell and Marina Gashinova

***Abstract*— The concept of sub-terahertz (sub-THz) imaging and recognition of space objects by a satellite based inverse synthetic aperture radar (ISAR) is proposed and analyzed in this paper. Operation at sub-THz frequencies in the band 200 GHz - 400 GHz benefits from wide available bandwidth, high sensitivity to surface texture and very small target features, and requires an antenna of small physical size. A feasibility study is presented based on use case scenarios of the relative motion of monitoring satellite and observed objects. Expected resolutions, power budget and oscillator stability requirements in this frequency band are discussed. Image formation methods are proposed and evaluated with simulations. A simple electromagnetic modeling capability is proposed to create a comprehensive dataset of sub-THz ISAR images, with the orientation and aspect angles seen by the sensors, which can be used to train semantic classifiers.**

***Index Terms*— Sub-THz, ISAR, space-borne radar, space object recognition**

I. INTRODUCTION

SPACE situational awareness (SSA) is vital for safety and security [1-5]. One of the aims of SSA is the surveillance and tracking of man-made objects in space, such as active and inactive satellites, discarded launcher stages and fragmented debris orbiting around the Earth. Of paramount importance is the early detection of potential hazards to space-borne assets. In particular, there is the need to protect satellites from both unintentional threats caused by the proliferation of debris and from deliberate threats posed by hostile satellites, missiles or objects spawned from them. Therefore, it is important to detect any changes in the appearance or in the behavior of active satellites indicating possible failures, which can have serious consequences. In order to verify changes of state of the satellite, for example caused by mechanical malfunction, it is desirable that regular assessments of the satellites' motion should be performed.

Large ground-based radars have historically been the backbone of SSA, providing high detection probabilities at long ranges and the ability to track several objects at one time. Examples of such radars are the German Tracking and Imaging Radar (TIRA) [3] and the radars in the US Space Surveillance Network [1]. Since they are ground-based they are best suited for observing objects in Low Earth Orbit (LEO). Since they are large and expensive many different surveillance demands will compete for their finite resources of surveillance time and look direction. The reducing cost of satellite launches means that in coming years space-borne radars [4-5] might be lower cost than the use of ground-based assets, while the radar design will certainly be simpler. Therefore, space borne radars installed on LEO to GEO satellites will be used for surveillance of a sizeable segment of space and benefit from a dedicated field of view. For instance, if the satellite carrying the radar, hereinafter the 'Monitoring Satellite,' (MS) is in a higher orbit than the 'Observed Satellite', (OS) it can view it from the side which is invisible to an earth-based sensor. Space-based operation also allows the use of higher frequency bands, because atmospheric absorption is no longer important.

Significant features of space objects are often much smaller than a meter across, so their characterization requires sensors with very high resolution. Since differential Doppler frequencies from different parts of the target can be measured, very good cross-range resolution independent of the range can be obtained using Inverse Synthetic Aperture Radar (ISAR) techniques [6]. Such a high resolution radar can be used to produce imagery with two potential outputs:

i. Resolving sets of bright points which, by their arrangement, will give an indication of the shape of the object which can be used as an input to a classifier. This is classic imaging ISAR.
ii. Detecting the backscatter from extended rough surfaces, which will allow image segmentation and 'joining the dots' in the clusters of bright points provided by (i). This requires the use of sub-THz frequencies to see these diffuse returns.

The space-based system proposed in this paper thus exploits an emerging technology in the sub-THz band around 200 GHz to 400 GHz, i. e. centered on 1 mm wavelength, and uses the motion of the target to provide two-dimensional imaging using the ISAR technique. A key benefit is the ability of sub-THz waves to sense texture and very small features of an object. The use of these frequencies allows a range resolution of the order of one centimeter to be obtained without requiring an excessive relative bandwidth. The use of very short wavelengths also allows a narrow beamwidth to be obtained from a compact antenna. A narrow beamwidth helps ensure that there are not overlapping targets in the field of view.

This paper describes the concept of sub-THz ISAR in space with resolution of the order of centimeters at ranges up to 100 km. This is superior performance than can be achieved from an optical sensor of similar size, weight and cost and also provides the additional benefit of robustness to lighting conditions, so imagery will be achievable from the dark side of the observable objects, or with the sun behind the object.

Such high resolution radar will be able to deliver a suitable input (closer to familiar video) into the processing stage designed to characterize, recognize and discern essential information about the state and intent of monitored objects, which however is outside the scope of this paper. Here we focus

on the concept viability and look at the challenges of focusing ISAR image to deliver data about both the point features and the distributed returns from extended surfaces.

A. Sensitivity to surface roughness.

The ability to detect texture is determined by the sensitivity of very small wavelengths to irregularities of similar order resulting in significant diffuse scattering. For example, recent results reported in [7, 8] demonstrate that (i) surfaces, "smooth" at low frequencies became "rough" at sub-THz frequencies and (ii) even a slight difference in roughness leads to contrast between surfaces in the imagery, owing to different backscattering returns, which can be effectively used for image segmentation.

B. ISAR

While the inherently large bandwidth, B, of sub-THz radar leads to fine range resolution, $\Delta R = c/2B$, the fine cross-range resolution is achieved by using the ISAR technique, where two-dimensional imagery of objects will be obtained by using their rotational motion relative to the radar operating frequency f_c:

$$\Delta X = \frac{c}{2 f_c \Omega} \tag{1}$$

where Ω is the total rotational span, or integration angle. Such rotation is related to either their own internal rotation or by their motion across the field of view of the radar, which causes the target's aspect to the radar to change (Fig. 1).

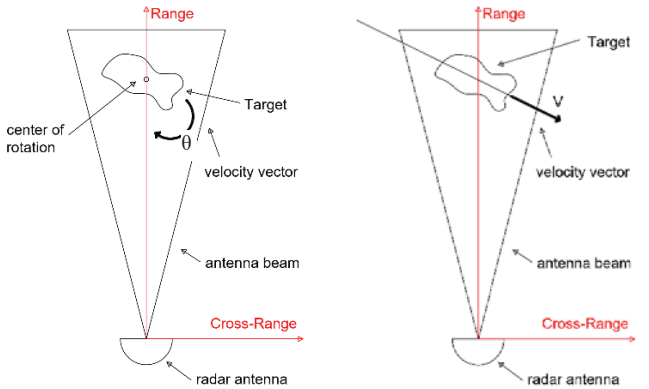

Fig. 1. Geometry of ISAR with the target rotating (a) or translating (b) within the antenna beam

The paper is organized as follows. Section II describes the concept of the proposed radar system. Section III examines its feasibility, including the calculation of sensitivity. Section IV outlines the simulation approach and examines how the ISAR image would be formed on the basis of simulated images. Two appendices are included to justify the facet size used in simulation and to calculate expected Noise Equivalent RCS of surfaces to be resolved by the proposed ISAR. The final section draws conclusions and suggests directions for future work.

II. Concept of Sub-THz ISAR Satellite Deployment

The feasibility study in Section III will demonstrate that an ISAR satellite payload could be used for a satellite in any orbit ranging from LEO to Geosynchronous orbits (GEO) to survey the space segment within a distance of 100 km.

We assume that the sub-THz sensor will be steered onto the object to be imaged using ephemeris data on the target which would be provided by other sensors, for example the global network of ground-based SSA radars. The system will provide imaging data which will supplement that obtained from ground-based sensors.

An examination of the distribution of satellite orbits [9] shows that many are clustered at altitudes around 780 km, which could be imaged by a sensor with a range of 100 km. Other clusters of orbits are around 400 km and geosynchronous orbits around 36,000 km, and in these cases the clustering means that they can all be reached from a sensor on the satellite within a range of 100 km from the mean altitude of each cluster. This range capability means that most satellites can be imaged with a small number of observation satellites.

Estimates of power budget and system parameters will be made based on current technology maturity. In this section we will present a concept of sub-THz radar sensing for space from space observation as a case study, based on the parameters derived in section III. This case study will outline the main features and benefits of using such a system in space.

A. Initial resolutions estimate

Without loss of generality we will consider a LEO satellite orbiting Earth at around 780 km from its surface. The following parameters will be used: detection range of 100 km, antenna diameter of 30 cm; operating frequency is nominally 300 GHz, so that the beamwidth of the antenna will be about 0.23°. The choice of a frequency of around 300 GHz has been discussed above. This also allows a signal bandwidth of 20 GHz to be readily achieved [10], giving a range resolution of about 1 cm.

The system concept is that the antenna is pre-positioned to observe the target as it crosses the beam. It can be pre-positioned based on ephemeris data on the target which can be provided by other sensors, such as ground-based SSA radars. The antenna must be able to be turned to point in the direction of the target, but this can be done relatively slowly. The antenna may then track the target as it crosses the field of view, but another version of the concept is that the antenna then stays fixed during the imaging period, to avoid the need for tracking in real-time. The target can be observed for the whole time while it is in the beam so the maximum integration angle, Ω, in equation (1) can then correspond to the antenna's physical beamwidth, which is approximately λ/d, where λ is the wavelength and d is the antenna width. Thus from (1) the best cross resolution can be estimated as:

$$\Delta X = \frac{d}{2} \tag{2}$$

This is the same value as is obtained for a strip-map SAR, although the derivation is rather different. For the proposed antenna of 30 cm diameter the cross-range resolution is of the order of 15 cm. More exact values will be calculated below.

This resolution might be improved and reduced to 1 cm, by taking advantage of any internal rotation or wobbling of the target and/or by using antennas with a wider beam (in the order of 2°), in this case the lower gain of the antenna will be compensated by an improved integration gain.

B. Use cases

This section discusses scenarios of observation of satellites

from the Monitoring Satellite which hosts the sub-THz radar. The objective is to estimate the range of available observation times, aspect angles and orientations depending on the relative motion of the MS and the Observed Satellite. From this we will be able to deduce the parameters which control the formation of the ISAR imagery.

In our analysis we will consider two LEO use cases, which define boundary values of observation time (slowest and shortest observation times), and, thus, ISAR resolution and power. Such use cases are used for demonstration of concept viability, and are not limiting assumptions on potential deployment of ISAR system.

Therefore we will assume here:

i. The orbits are circular;

ii. MS and OS are within the same orbital plane, and either move in the same direction (co-rotation) or opposite direction (counter-rotation). This assumption defines extreme values of the observation times, as shown later in section 2, though does not reduce the generality of the concept;

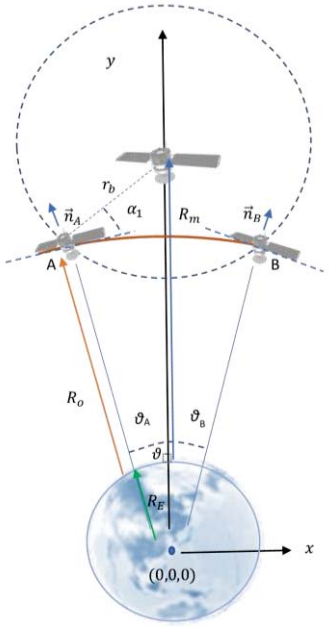

Fig. 2. Estimation of change of orientation and viewing angle of object during observation time

Fig. 2 shows a sketch of the scenario where the MS is above the OS. In this case, the OS is observed from a side not visible from the earth and its most prominent visible feature is represented by the solar panel wings. In the opposite situation, when the MS is below the OS, the latter is observed from the side of antennas directed toward the earth, this will allow assessment of the state of the antennas and structure of the bus. In the sketch in Fig. 2:

- R_m and R_o are the orbital altitudes of the MS and the OS, r_b is the radius of the detection volume centred at the MS.
- R_E=6371 km is the radius of Earth.
- $\overrightarrow{n_{A/B}}$ is a vector normal to the tangent to the circular orbit. This vector shows orientation of the OS with respect to (w.r.t.) the Earth and to the MS when entering and exiting the surveillance basket at points A and B, respectively.
- $\alpha_{A/B}$ and $\beta_{A,B}$ (complimentary to $\alpha_{A/B}$) are the aspect and look angles, respectively, at two extreme points A and B;
- $\theta = \angle(\mathbf{n}_A - \mathbf{n}_B)$ indicates the change of orientation of the OS w.r.t. Earth and, importantly, its orientation w.r.t. the MS when it translates through the detection basket of the MS.

1) Orientation of the OS with respect to the MS

The trajectories and orbital planes of the MS and the OS are:

$$\begin{cases} x^2 + y^2 = \left(R_m + R_E\right)^2 \overset{\text{def}}{=} R_M^{\,2} \\ z = 0 \end{cases} \text{ and } \begin{cases} x^2 + y^2 = \left(R_o + R_E\right)^2 \overset{\text{def}}{=} R_O^{\,2} \\ z = 0 \end{cases} \quad (3)$$

The points A and B are defined as an intersection of circles of the OS orbit and the MS detection volume within the same orbital plane:

$$\begin{cases} x^2 + \left(y - R_M\right)^2 = r_b^{\,2} \\ x^2 + y^2 = R_O^{\,2} \end{cases} \Rightarrow \begin{cases} y_A = y_B = \dfrac{R_O^{\,2} + R_M^2 - r_b^{\,2}}{2R_M} \\ x_{A/B} = \pm\sqrt{R_O^{\,2} - y_{A/B}^{\,2}} \end{cases} \quad (4)$$

The normal vectors to the OS at the interception points are:

$$\frac{y}{y_A} = \frac{x}{x_A} \quad \text{and} \quad \frac{y}{y_A} = \frac{x}{x_B} \quad (5)$$

Therefore, the orientation angles are:

$$\begin{cases} y^{(1)} = x\dfrac{y_A}{x_A} \\ y^{(2)} = x\dfrac{y_A}{x_B} \end{cases} \Rightarrow \begin{cases} \theta_A = \arctan\left(\dfrac{y_A}{x_A}\right) \\ \theta_B = \arctan\left(\dfrac{y_A}{x_B}\right) \end{cases} \quad (6)$$

The aspect angles, α, at which the OS is seen by the MS are:

$$\begin{cases} \alpha_A = \arctan\left(\dfrac{R_M - R_O}{x_A - 0}\right) - \theta_A \\ \alpha_B = \arctan\left(\dfrac{R_M - R_O}{x_B - 0}\right) - \theta_B \end{cases} \quad (7)$$

Results for illustrative example with satellites in LEO orbit, with the MS at 780 km orbital altitude observing satellites at lower altitudes, in the range 680-780 km, are shown in Fig.3. Importantly, the red curve in Fig. 3.a shows total rotational span, Ω, equal to a change of aspect angle, α, of the OS while passing the detection basket of the MS, which later in sub-section 3) of this section will be used for correction of the expected cross-range resolution.

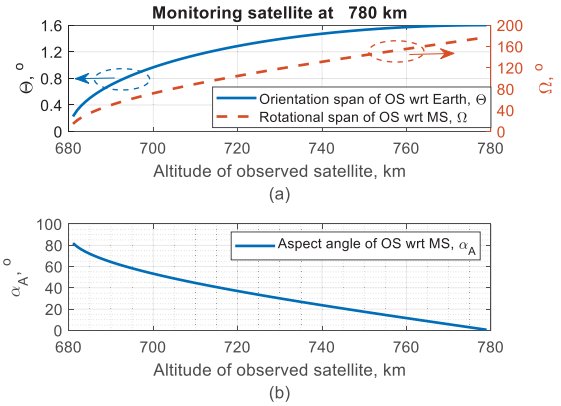

Fig. 3. (a) Total change of orientation angle of OS wrt Earth as function of distance between MS and OS (blue solid line); angular span of rotation of OS wrt MS (red dashed line) (b) aspect angle of OS wrt MS at point A

2) Observation time of the OS with respect to the MS

When the OS enters the detection basket, its relative velocity w.r.t. the MS is the difference between orbital velocities of the MS and the OS:

$$v_{rel} = |\mathbf{v_O} - \mathbf{v_M}|, \quad \mathbf{v_O} = \sqrt{\frac{M \cdot G}{(R_o + R_E)}} \cdot \mathbf{e_o} \quad \mathbf{v_M} = \sqrt{\frac{M \cdot G}{(R_M + R_E)}} \cdot \mathbf{e_M} \qquad (8)$$

where $\mathbf{e_o}$ and $\mathbf{e}_M$ are directional velocity unit vectors of OS and MS, respectively, M=5.976·10^{24} kg is the mass of Earth, G=6.67·10^{-11} N·m^2/kg^2 is the Gravitational constant. Therefore, the OS will stay within observation volume for approximately:

$$t_{obs} \approx \frac{\|\mathrm{A,B}\|}{v_{rel}} \qquad (9)$$

Now consider two cases of mutual motion of both satellites: (i) co-rotation and (ii) counter-rotation. These define two extreme values of the total observation time of the OS, the longest and shortest possible, while for different orbital planes of the OS and the MS the values will be intermediate.

Considering the same example with LEO satellites we will have the orbital velocity of 7.47 km/s for the MS at 780 km altitude and that of the OS at 680 km will be 7.52 km/s. Therefore v_{rel}=0.05 km/s if both the MS and the OS satellites are co-rotating, and v_{rel}=15 km/s if they move in opposite directions (counter-rotating), resulting in significant differences in observation times between each case.

Estimates of the total observation time as function of the altitude of the OS are shown in Fig. 4 for (a) co-rotation; (b) counter-rotation.

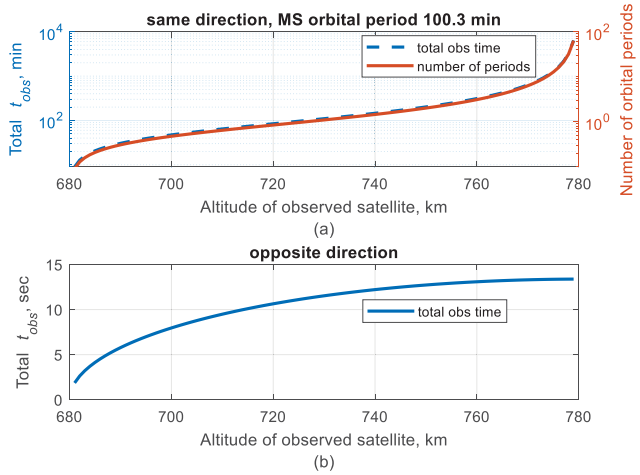

Fig. 4. Total observation time as function of altitude of OS for cases of MS and OS moving in (top) same directions (vertical axis units in min) and (bottom) opposite directions (vertical axis units in sec)

In case of different orbital planes, the relative velocity of OS w.r.t. MS is:

$$v_{rel} = |\mathbf{v}_O - \mathbf{v}_M| = \sqrt{v_O^2 + v_M^2 - 2v_O v_M \cos\phi} \qquad (10)$$

where angle ϕ is an angle between velocities of the satellite. Fig. 5 shows the total observation time as function of the altitude of the OS calculated for different ϕ.

For the fixed beam antenna which is pre-positioned to where the OS enters the detection basket, the observation time will be between times for two considered extreme cases: the slowest observation time, related to co-rotating motion (angle= 0 between velocity vectors) which is about 15 secs and the shortest time for counter-rotating motion (angle 180º) , which is about 27 ms.

According to Fig. 5 above for most of the angles (180-10 degrees) the observation times will be within 27 ms secs to 310 ms at 100 km orbital altitude difference, which are very suitable for ISAR imagery.

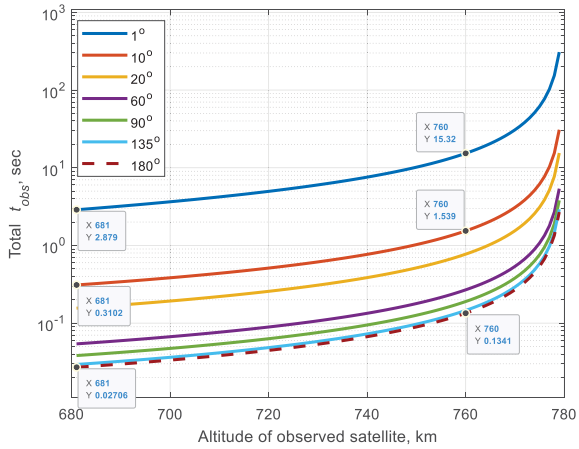

Fig. 5. Total observation time as function of altitude of OS for different angles between velocities of the satellite

It is worth stressing here that, in the case of co-rotating motion, the MS will stay above the OS for a significant time, for instance when the OS is at 60 km distance from the MS it will be "seen" by the MS for nearly one orbital period while for closer satellites the observation time may well be within several periods. In such cases the OS and the MS satellites practically do not change mutual positions during typical ISAR imaging times, which will negatively impact the achievable cross-range resolution. The long integration times are however very favorable for the power budget, but the resulting very low Doppler shifts mean that the system will be very sensitive to the oscillator stability close to carrier. For all these reasons, for the feasibility analysis in section III we will consider the satellites moving in opposite directions as use case.

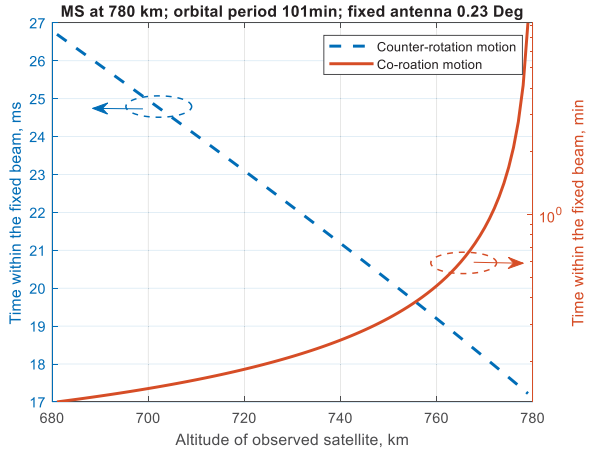

Fig. 6. Observation time (time for OS to pass through the fixed beam of MS) as a function of the altitude of OS.

Considering a fixed (not tracking) radar antenna of finite beamwidth, Θ. the observation time will be reduced by a factor $K = (\beta_A - \beta_B)/\Theta$, so that the minimum observation time will be $t_{obs}^{fixed\ beam} \approx t_{obs}^{tot} / K$. Fig.6 shows the plot of the observation

time as a function of the OS altitude for the same illustrative example of Fig. 4 and fixed antenna of Θ=0.23°.

The observation time is required for both the radar power budget calculation and the estimation of the effect of the oscillator noise sidebands on the images. For the investigation of the concept viability it is sufficient to use a single typical value for this in further analysis. A value of 20 ms will therefore be assumed for the observation time in section III.

3) ISAR resolution

The goal is to estimate the upper boundary of achievable resolution. Initially we assume availability of the whole aperture if the MS antenna is tracking the OS, so that observation time equals the duration of the OS being within the detection volume of the MS. Then it can be reduced to whatever beam we use in case of fixed antenna.

Using, as evaluated in the previous section, the total angular span of rotation of the OS w.r.t. the MS, Ω, (equal to $2\beta_{A/B}$) we can estimate the cross-range resolution (1) for: (i) the whole available observation time (equivalent to the tracking antenna within the detection volume), shown in Fig. 7(a); (ii) for the fixed antenna defining a limited field of view, in Fig. 7(b). Figures 7(a) and 7(b) are of course complementary since if a tracking antenna is used, the cross-range resolution is only a function of the scan angle during the dwell and not of the physical beamwidth.

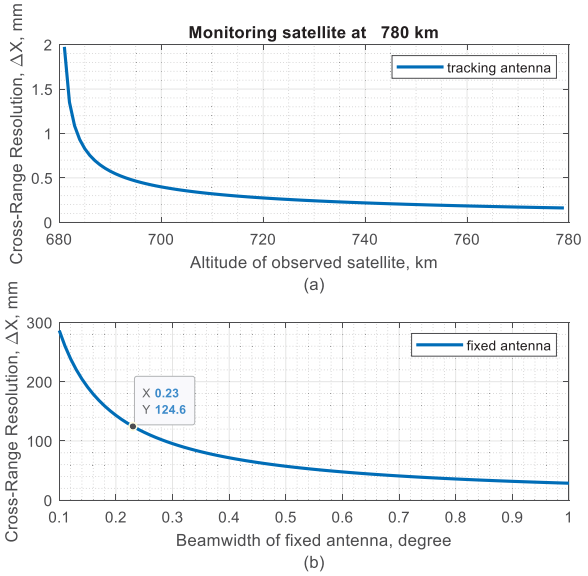

Fig. 7. Estimation of cross-range resolution, ΔX, for (a) MS antenna tracking OS within the MS detection basket as function of OS altitude, (b) fixed antenna as function of antenna beamwidth

In case of the fixed antenna of 0.23° beamwidth the cross range resolution would be about 12 cm, which agrees well with initial estimates in Section II.A. It is worth mentioning here that there will be also changes of the duration within the fixed beam antenna depending on the pointing direction of antenna within the detection basket with the longest time being for the points A and B. As can be seen from Figure 2, however, if the monitoring radar beam looks down towards the earth, the attitude of the satellite will change relatively rapidly as it crosses the beam, compared to the cases A and B where the radar beam is looking at a much shallower depression angle. The changes due to these two trends will largely cancel each other out and so will result in only a slight change of the expected cross range resolution per direction of fixed beam antenna.

III. FEASIBILITY

As discussed above, the analysis in this section will consider the case where the satellites are moving in opposite directions.

A. Power budget

In order to achieve 100 km range against typical space objects we will see that the radar will need a mean power of some tens of watts. This power is likely to be available from Travelling Wave Tube (TWT) transmitters. Such tubes are currently under development at these frequencies. Design studies, such as [11] have suggested that a continuous power of 80 W would be possible at 220 GHz. The sensitivity calculation will assume, conservatively, that this will be reduced to 40 W peak at 300 GHz.

In order to handle this level of mean power the radar should operate in a pulse-compressed mode. Since the range to the target will be known a priori from ephemeris data the waveform can be assumed to have a 50% duty cycle with the pulse repetition interval being optimized so the receiver is open over the time of reception of the pulse from the range of the target.

The sensitivity calculation is based on the free space radar equation:

$$SNR = \frac{P_t G^2 \lambda^2 \sigma}{(4\pi)^3 R^4} \frac{1}{kT_s B_i N_f} \qquad (11)$$

where the parameters are assumed to have the following meanings and values: P_t is the mean transmitter power of 20 W; λ is the wavelength, 1 mm at 300 GHz; G is the antenna gain, equal to approximately 57 dB for the suggested antenna diameter of 30 cm; SNR is the signal to noise ratio required for detection which may be taken as 15 dB; $R = r_b$ which in this system design is 100 km; σ is the radar cross section (RCS) of the smallest detectable target at 100 km; k is Boltzmann's constant; T_s is the nominal system noise temperature which may be taken as 300 K, as is conventional practice, more detailed study might consider the effect of different physical temperatures; B_i is the effective noise bandwidth taken as 50 Hz, the reciprocal of the typical observation time estimated in section II; N_f is the system noise figure at the temperature Ts. It is assumed that a noise figure of 5 dB will be practical for future systems at this frequency. This is 3.6 dB better than that quoted by Tessmann et al. [12] for a complete receiver front end, but makes allowance for anticipated technological developments over the next few years before the proposed system would be launched.

The assumed antenna gain takes account of the likely efficiency of a practical antenna.

The SNR is estimated as that which is needed for the whole target to enable imaging. The SNR within individual pixels within the image may be significantly lower and still be useful. As an example, the image may consist of ten significant reflecting regions each with an SNR of 5 dB.

The minimum detectable RCS can be calculated by inverting (10), giving a value of -1 dBm^2 for the whole satellite.

If the pixel size is based on the cross-range resolution of 12cm, also taken from section II, and the pixels are assumed to be square then the specific RCS corresponding to the noise floor (the noise equivalent specific RCS) is +2 dBm^2/m^2. This is an indication of the minimum total RCS of extended targets which can be detected. We can increase the range resolution without losing significant sensitivity because imaging techniques will tend to perform a process akin to integration over the total number of pixels containing the image, which will largely compensate for the fact that the power is split across a greater number of range cells, so an effective pixel size comparable with the square of the cross-range resolution, as used above, is appropriate for estimating the sensitivity for target recognition.

B. Oscillator stability and cross-range sidelobes at 300GHz

The frequency stability of the transmitter oscillator limits the ultimate resolution that can be achieved by any Doppler-based processing, such as ISAR, which measures the phase differences between successive measurements. In ISAR systems, the transmitter's frequency modulated (FM) noise spectrum is effectively convolved with the cross range point spread function, with the proviso that any noise which is correlated with the receiver local oscillator is suppressed by a factor of [13]:

$$C = 4\sin^2\left(\pi f_m \delta\tau / 2\right) \tag{12}$$

where f_m is the frequency offset from the carrier and $\delta\tau$ is the time of flight of the signal to the target and back.

The average value of $\sin^2(x)$ is ½, so the average value of C is 2. For values of $f_m \cdot \delta\tau$ less than ½ the value of C is less than this and the noise is partially suppressed. At the maximum range of 100 km (a delay of 666.7 μs), this correlation occurs for frequency offsets below 750 Hz. The modeling will take this factor into account. For higher offsets the values oscillate and the noise levels are generally lower so the detailed behavior is less significant, so the mean value of 2 will be used.

This section discusses the transmitter stabilities which are likely to be achievable at 300 GHz and analyses the effect which these would have on the dynamic ranges of the proposed ISAR system, with a range of 100 km and an integration time of 20 ms, as derived in section II.

1) Scaling FM Noise Levels with Carrier Frequency

Since 300 GHz sub-system technology is undergoing rapid development, the levels of oscillator FM noise levels at 300 GHz which will ultimately be available are better obtained by extrapolation from the performance of oscillators at lower frequencies than from the characteristics of currently-available 300 GHz oscillators.

One way to perform such an extrapolation is to consider that if the 300 GHz signal is obtained by multiplying-up a lower frequency oscillator by a ratio ρ then the FM noise density at a given modulation frequency will be increased by the same factor. If the deviation, Δf, is much less than the modulation rate then the noise at an offset fm from the carrier will be derived from the noise at the same modulation frequency. From [14] the single sideband (SSB) FM noise density at the offset f_m will be:

$$P_f = \frac{\left(\Delta f / f_m\right)^2}{4} \tag{13}$$

If the oscillator frequency is multiplied up by a factor ρ then the FM noise levels at given offsets will thus be multiplied up by a factor of ρ^2.

An alternative view is to consider a fundamental oscillator at 300 GHz. In this case we may employ the following equation, derived from [15], as a basis for estimating the FM noise levels:

$$P_f = \left(\frac{M \cdot kT_0 B}{2P_0}\right)\left(\frac{f_0}{Q \cdot f_m}\right)^2 \tag{14}$$

where M is the noise figure of the oscillator's sustaining amplifier, T_0 is its absolute temperature, B is its bandwidth and P_0 is its output power, so the factor $M \cdot kT_oB/2P_o$ is the reciprocal of the signal noise ratio of the signal fed back into the amplifier. Q is the quality factor of the oscillator's resonator and f_0 is the frequency of the oscillator.

This again leads to the conclusion that, other things being equal, the noise levels will be proportional to the square of the frequency of the oscillator. In practice this is true for oscillators over a wide range of frequencies and again supports the procedure for predicting the FM noise levels at 300 GHz from those of oscillators at lower frequencies by assuming that the noise power densities increase by ρ^2.

Note also that if the underlying frequency noise density, Δf, is independent of f_m then the FM noise density will be proportional to $1/f_m^2$. In this case the increase in noise density caused by increasing the carrier frequency by a factor ρ can be counteracted by increasing the offset from the carrier by the same amount. In fact, the dwell time to obtain a given cross-range resolution will be reduced by this factor, ρ, because the Doppler frequencies all increase by the same ratio, so everything would just scale by this factor.

The oscillator's stability will be improved by locking it to a lower-frequency source, so the complete FM noise model for the oscillator will contain the following factors:

i. At high offsets from the carrier, outside the bandwidth of the locking circuits, the FM noise will follow a $1/f_m^2$ law as expected from (13);
ii. Within the locking bandwidth the FM noise level will be flat, until we get sufficiently close to the carrier for it to start to rise again at a rate of a $1/f_m^2$ as the locking gain become insufficient to overcome the rising intrinsic noise of the oscillator;
iii. At frequencies below ~1 kHz from the carrier the noise will start to rise at a faster rate of $1/f_m^3$ due to flicker noise in the devices;
iv. Very close to the carrier, at deviations of 1 Hz or less, the noise spectrum is better modelled as a Gaussian, but this region is not important for the ISAR system being considered here.

2) Expected stability of future 300 GHz transmitters

As discussed above, the stability which will be obtainable by future 300 GHz transmitters can be predicted from performance at lower frequencies. A good baseline is the 2LPL series of phase locked oscillators manufactured by L3 – Harris [16]. The performance of an oscillator at 14.84 GHz can be extrapolated to 300 GHz using ratio $(f/f_0)^2$, deduced above where f = 300 GHz and f_0= 14.84 GHz.

Table 1. Expected Noise Density at 300 GHz – Electronic Oscillator

Offset from Carrier, kHz	*Single Sideband FM Noise Density, dBc/Hz*
0.01	-15
0.1	-49
1	-66
10	-71
100	-72
1000	-89

Reference [17] reports the FM noise for an oscillator using opto-electronic (laser) based devices. The oscillator operates at 10 GHz but the FM noise levels extrapolated to 300 GHz are shown in Table 2:

Table 2. Expected Noise Density at 300 GHz – Opto-Electronic Oscillator

Offset from Carrier, kHz	*Single Sideband FM Noise Density, dBc/Hz*
0.01	-25
0.1	-60
1	-90
10	-115
100	-120
1000	-130
10000	-150

3) Estimated performance

The 20ms integration time noted in section II implies a frequency resolution of 50 Hz, which will correspond to the cross-range resolution of 0.12 m. The frequency/distance relationship is thus 2.4m/kHz. If the largest object is 7.5 m across, we thus have to consider noise at Doppler offsets in the range 50Hz (1 cross-range cell) to 3kHz.

a) Electronic oscillator

The effective noise levels at the frequencies relevant to ISAR imaging are shown in Table 3:

Table 3. Dynamic Range Limitation due to FM Noise – Electronic Oscillator

Offset from Carrier, kHz	*s.s.b Noise, dBc/Hz*	*Noise in Resolution Bandwidth, dBc*
0.05	-40	-43
0.1	-49	-46
0.3	-59	-46
1	-66	-46
3	-69	-49

The noise in the resolution bandwidth is calculated by multiplying the noise per unit frequency by the correlation factor from equation (11) and by resolution bandwidth.

b) Opto-Electronic Oscillator

The effective noise levels for the electro-optic oscillator at the frequencies relevant to ISAR imaging in this case are shown in Table 4:

Table 4. Dynamic Range Limitation due to FM Noise – opto-electronic Oscillator

Offset from Carrier, kHz	*s.s.b Noise, dBc/Hz*	*Noise in Resolution Bandwidth, dBc*
0.5	-49	-52
0.1	-58	-55
0.3	-73	-60
1	-88	-68
3	-103	-83

4) Conclusions Regarding Oscillator Stabilities

The use of electronic oscillators can be expected to give a dynamic range of 46 dB at frequency offsets corresponding to cross range distances greater than 1 m from a bright scatterer and up to 49 dB over the full length of the target. An electro-optic oscillator might be able to give a significantly better dynamic range, but the dynamic range available from an electronic oscillator will probably be perfectly adequate.

Another important conclusion which can be drawn is that the effective noise floor close to a large target is usually independent of the Doppler resolution. As discussed above, close to the carrier, the phase noise is expected to be dominated by flicker noise, i. e. to follow a $1/f_m^3$ law. Close to the carrier however, this noise is also partially correlated between transmitter and receiver, and the decorrelation follows a f_m^2 law. The net effect is that the noise density in the image will follow a $1/f_m$ law. If, for example, the cross-track velocity of the target increases so the Doppler shift corresponding to a given cross-range distance increases the increased offset from the carrier will lead to a proportional reduction in the FM noise density seen at the image. On the other hand, the faster motion will lead to a corresponding reduction in the integration time and thus an increase in the Doppler bin width, so the perceived FM noise level per bin will remain unchanged. Therefore, within the important region where the noise is dominated by flicker noise but is correlated between transmitter and receiver, the noise power per cell, and hence the dynamic range, are unaffected by changes in the integration time.

IV. ISAR IMAGE FORMATION METHODS

There is an extensive literature on ISAR image formation, see for example [6] and the reason for re-visiting the algorithms here is to propose those which are most appropriate for the image formation from sub-THz data from space objects. One difference from many SAR/ISAR applications is that we can obtain very fine cross-range resolution combined with the narrow real-aperture beamwidth. This is a function of the high proposed carrier frequency and reduces the probability of multiple targets appearing within the beam. Another difference is the ballistic motion of the objects being imaged, which is a consequence of that fact that we are observing orbiting objects in space. This difference should simplify image formation.

A. Image formation algorithm

Considering the geometry in Fig. 1, the signal $S_R(f,t)$ received from a target, which may have both translational and rotational motion, can be modelled as [6]:

$$S_R(f,t) = S_T(f)e^{-j2k_r(t)r(t)}\iint \psi(x,y)e^{-j2\pi\left(xk_x(t)-yk_y(t)\right)}dxdy \quad (15)$$

where $S_T(f)$ is the Fourier transform of the transmitted signal, $r(t)$ is instantaneous range to the geometric center of the target, $\psi(x,y)$ is the target reflectivity function which is to be reconstructed, k_x and k_y are the components of the spatial frequency $k_r = 2\pi f / c$.

In general, an image reconstruction comprises of three stages:

1. Motion Compensation: $S_R''(f,t) = S_R'(f,t)e^{j2k_r(t)r(t)}$

Where $S_R'(f,t) = S_T^*(f)S_R(f,t)$ is the range compressed signal.

2. Image formation: $\psi(x,y) = \iint S_R''(t,f)e^{j2\pi\left(xk_x(t)-yk_y(t)\right)}dtdf$

3. Image processing

To follow the proposed algorithms to implement these three stages:

1) Motion compensation

For targets with translational motion, scatterers appear at different positions in different range profiles, this is the major cause of defocusing in ISAR images and this effect needs to be compensated. The radial motion compensation comprises of two steps. Firstly, the alignment of range profiles is performed thorough the Entropy minimization method.

After the range profiles have been aligned, the second step of the motion compensation stage, made using Phase Gradient Autofocus (PGA), aims to remove the residual phase error caused by the phase drifts in the range profiles which still cause defocusing in the image.

The following sections describe the Entropy minimization and PGA algorithm:

a) Entropy minimization

The entropy function can be used as a cost function to align range profiles and adjust phase functions in ISAR. The amount of each profile shifts relative to the one that precedes it, is computed iteratively to minimize the entropy of the average range profiles, as defined in [18]. If range profiles are accurately aligned then the entropy should reach the minimum value. As the range shift is evaluated for the consecutive profiles, it describes a range function which is smoothed by fitting it to a low order polynomial, so that the gradual change is constant, obtaining a linear function which is used to correct the phase of the received signal.

The use of the average range profiles and a global quality measure, like the entropy, is suitable for ISAR images made with very small wavelength and high range resolutions, where the reflection from the target is spread in all the resolution cells occupied by the target and dominant point scatterers, required by other focusing schemes, may not be present.

b) Phase gradient autofocus

The phase adjustment is made applying the PGA algorithm [6]. If a complex target has no stable prominent scatterer point, the phase gradient (i.e. phase difference from pulse to pulse) can be estimated by measuring the pulse-to-pulse phase difference at each range cell and averaging them. Finally, the phase correction is made iteratively.

The iterative nature of the PGA allows robust and nonparametric estimation and exploits the redundancy of the phase-error information contained in the ISAR image, without the need of isolated point-like reflections, required by other autofocus algorithms (i.e. Prominent Point Processing) and which may not be present at sub-THz frequencies and high range resolution.

2) Image formation: Range-Doppler algorithm

When target-radar distance is larger than the far field distance of the target, the plane wave assumption can be used. Moreover, for translating targets after the motion compensation step and rotating with small integration angles, a simple range-Doppler (RD) processing can be used to produce the image. Under this assumptions, the RD method can be successfully implemented by means of a Fourier transform because the polar grid, in which the collected data is distributed, can be approximated by a rectangular grid.

3) Image processing: CLEAN algorithm

If there are strong scatterers present in the target image, the dynamic range of the focused image can be limited so it might be impossible to detect small targets in the vicinity of the strong ones, due to the sidelobes of the strong target masking the small ones. This can represent a problem for the scope of sub-THz ISAR, where the aim is indeed to sense small features of the targets. The CLEAN method [19] can help to solve this problem by reducing sidelobes of dominant scatterers. It works by identifying the brightest pixel in the image. The point spread function (PSF) of the brightest pixel is then subtracted and the location and intensity information is retained. Once the brightest scatterer is removed, the procedure is repeated with the next brightest source in the image until some predefined stopping criterion is applied.

Initial results of experimental ISAR imagery at 300 GHz obtained in controllable conditions can be found in the conference paper [20].

B. Simulations

Simulation of the returns which will be seen by the system are needed for three reasons. The most important is that since the system is intended to observe and automatically recognize the targets from directions other than that from the ground, the training data for the automatic recognition cannot be obtained from the ground. The classifiers must therefore be designed using synthetic data. In addition, obtaining the required quantities of training data from an actual radar would be an unfeasibly large task, even if it were physically possible.

The second reason for creating simulated images is to check whether the proposed recognition is likely to be practical.

The third reason is to provide data to support the detailed development of the image formation algorithms outlined above.

The two objectives of this sub-section are:

i. To illustrate the advantages of sub-THz waves to provide ISAR images resolving small features and outlining the shape of the object, based on the backscatter from extended rough surfaces at these frequencies, in addition to the set of bright scatterers as in traditional ISAR.
   Once the model is justified we can use it for the second objective:
ii. To obtain the dataset of expected images of satellites referring to aspect angles and orientations considered in the use cases in Section II, which are needed to train image based classifiers.

In both cases the scattering object is modelled by a set of point scatterers described by their locations in an object-centric coordinate system, the origin of which is at the geometric center of the target. We assume that the object moves along a straight line with an angle wrt the line of sight to the radar. The received signal is processed with an algorithm formed by the methods described above in sub section A: range-Doppler for the image formation, range alignment with the entropy minimization method, autofocus with the phase gradient autofocus algorithm.

1) Comparison of ISAR images of surfaces at 75 and 300 GHz generated by a facet model.

Sensitivity to rough surfaces is one of the main benefits of using sub-THz as it gives a means to see the whole extent of the object, as opposed to resolving only a set of bright points.

Appendix II evaluates Noise Equivalent RCS of expected surfaces to demonstrate the feasibility of resolving diffused returns from them, while here we focus on the ability of the simulator to sense the roughness.

Here we aim to demonstrate that a surface, which appears smoother at lower frequency, becomes rough at a higher frequency, resulting in higher backscattering, an ability to resolve small features and, therefore adequate surface profile reconstruction.

Simulations have been carried out using a high-frequency approximation of Maxwell's equations, i.e. ray optics. In fact it has been shown that the electromagnetic scattering from a complex target can be described by a set of localized reflections from discrete rays. The position of the scatterers in the target' coordinate system is determined by the intersection of a set of rays, which synthesize the wavefront, and triangular facets into which the surface of the target is decomposed [21]. The model does not consider multiple scattering.

As representative example, the target is a random uneven surface of 64 cm x 64 cm with maximum elevation of 0.8 mm. The surface is decomposed in isosceles triangular faces through the Delaunay triangulation, a technique for creating a mesh of contiguous, non-overlapping triangles from a dataset of points [22]. The size of the triangle's longest side is proportional to the wavelength (10λ) and is chosen to be smaller than the range resolution, so that the target reflects signal in all the resolution cells that it occupies. Fig. 8, shows the different sizes of the facets at 75 GHz and 300 GHz to decompose the surface.

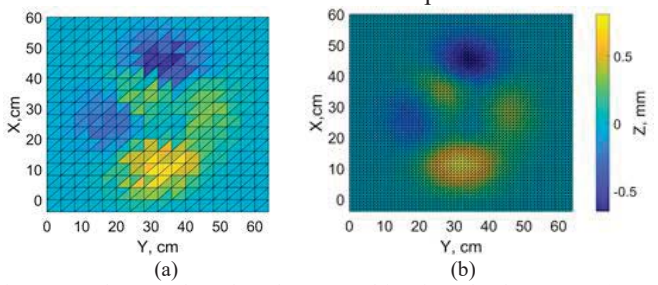

Fig. 8. Random rough surface decomposed in triangular faces at 75 (a) and 300 (b) GHz

The amplitude of the reflection for each face is function of the area of the triangle, the frequency and the incident angle.

The ray/triangle intersection is calculated using the Möller and Trumbore algorithm [23]: every point of the intersection on the triangle is expressed in terms of the distance from the center of gravity of the triangle *B* (Fig. 9). The incident angle θ is the angle formed by the vector of ray's direction and the normal to the triangle surface $\hat{n}$.

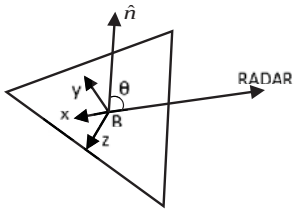

Fig. 9. Geometry of the RCS calculation of triangular face

The triangular faces are considered for simplicity as flat plates. The RCS of the face is [24]:

$$\sigma = 4\pi A^2 \left[\frac{\cos(\theta)}{\lambda}\right]^2 \frac{\sin^4(\beta/2)}{(\beta/2)^4} \qquad (16)$$

$\beta = (2\pi/\lambda) b \sin\theta$, b is the triangle longest side and A the area of the triangular face.

Table 5 illustrates the parameters used in the simulation, both for the target and radar. The number of facets is 64 (4^3) higher at 300 than at 75 GHz, the radar parameters for the ISAR simulation are chosen to have the same image resolutions at both frequencies.

Table 5. Parameters of the facet model simulation

Parameter		
Center frequency, GHz	300	75
Number of facets	8192	512
Range resolution, cm	1.5	1.5
Cross-range resolution, cm	1.7	1.7

For this part of the simulation a very fine cross-range resolution was used to obtain square pixels as a best way to demonstrate sensitivity to surface roughness profile.

Appendix 1 provides an analysis of the modelling of rough surfaces, which are locally curved, and shows that the faceting applied at both 75 GHz and 300GHz are adequate to represent the surfaces with the roughness characteristics (height and correlation length) modeled.

The results in Fig. 10 show that the ISAR image of the surface in Fig. 8, at 300 GHz (Fig. 10.b) comprises a more detailed and continuous image with the less reflective areas of the surface which are positively (convex) and negatively (concave) elevated, so their facets are retro-reflecting away from the source, while at 75 GHz (Fig. 10.a) only a few isolated reflecting points are seen.

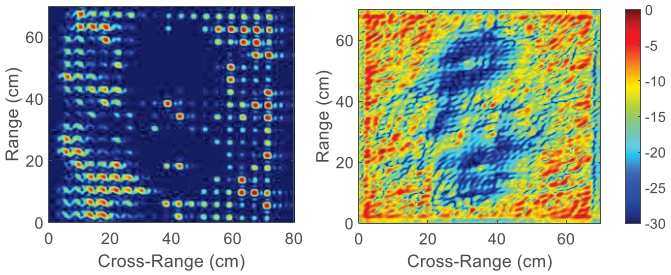

Fig. 10. ISAR images of the random rough surface at 75 (a) and 300 (b) GHz.

2) Expected images at 300 GHz using a satellite model

To produce the ISAR images of a satellite at sub-THz frequencies, a point-scatterer based model of the satellite Calipso (Fig. 11) has been built from a CAD model available at [25].

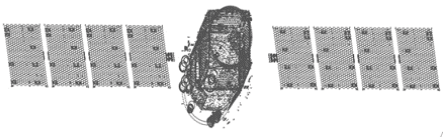

Fig. 11. Point scatterer model of Calipso satellite

The overall width of the satellite is about 8 m. The point-scatterer model is simple and helpful for studying algorithms of image formation, motion compensation and autofocusing. Moreover, it can be used to build a library of images needed to train classifiers to test classification algorithms based on machine learning.

The use of a very high number of points models the expected behavior of THz waves, which, as shown in the previous section, are able to sense reflections from a very high number of scatterers in a target. For this model the amplitudes of all the point scatterers can be made the same, so that there are no prominent point scatterers. This simplified model is suitable to test the effectiveness of the range alignment algorithm, the modified entropy minimization method, which uses the average range profiles, and autofocus algorithm based on the phase gradient method.

Table 6 summarize the parameters of the simulation, using radar and motion parameters determined in the use cases Section II/III, so that the target is at 100 km from the radar and moves at a velocity of 15 km/s (Fig. 12).

Table 6. Parameters of the ISAR simulation of the satellite point scatterer model

Parameter	
Center frequency, GHz	300
Range, km	100
Velocity, km/s	15
Angle of motion, deg	90
Range resolution, cm	2
Cross-range resolution, cm	15
Number of points of the model	75036

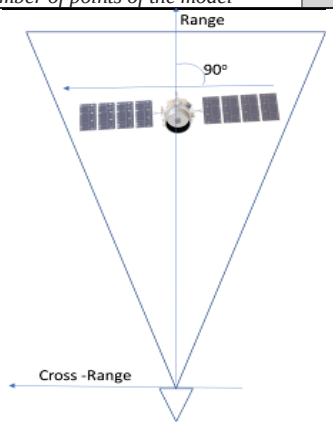

Fig. 12. Geometry of the simulation

a) Formation of the Images

The image was obtained without adding system noise, which can be easily added, but omitted at this stage for clarity of demonstrated effects. Fig. 13 shows the 300 GHz ISAR images produced at each step of the image formation algorithm.

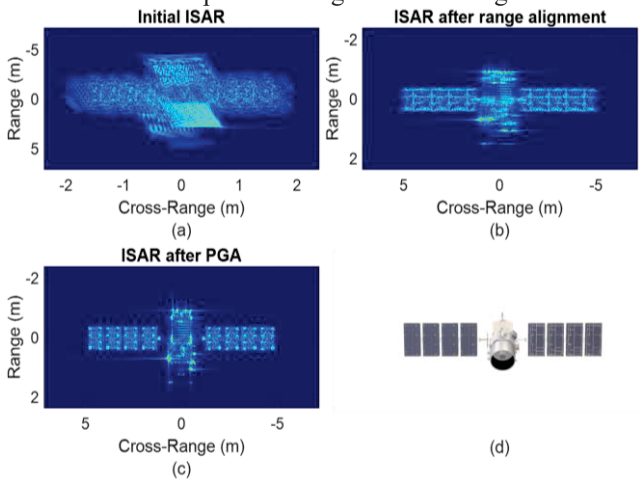

Fig. 13. 300 GHz ISAR image produced after each step of the image formation algorithm. (a) raw range-Doppler, (b) after range allignment, (c) after the phase corretion. (d) 3D model of the satellite

13.a is produced by processing the received ISAR raw data with the range-Doppler algorithm, with clear effect of range migration. In 13.b the range migration is corrected to keep the scatterers in the same range resolution cells, however the phase drift caused by the shifting in range cells causes the defocusing. 13.c is obtained by applying the PGA method for autofocus and shows all the details detectable in the optical image at the bottom right.

b) Comparison of expected images at 75 and 300 GHz

In Fig. 14 the simulated images at 75 GHz and 300 GHz are compared. These images are produced taking into consideration the results obtained from the simulation of a rough random surface in the previous section. The 3-dimensional point scatterer model of the satellite at 75 GHz is obtained by under-sampling the model used for the 300 GHz simulations, shown in Fig. 11, by a factor 64 (4^3).

As these results show, at 75 GHz only few scatterers will contribute to the formation of the ISAR image (Fig. 14.a), while at 300 GHz an image close to the optical image is expected.

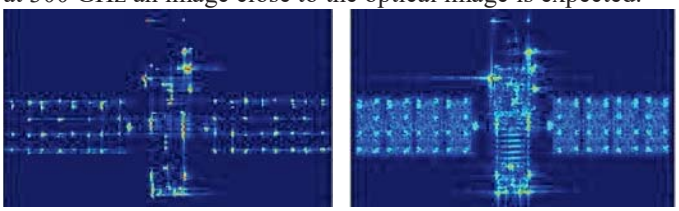

(a) (b)

Fig. 14. Expected ISAR images from a satellite target at 75 (a) and 300 (b) GHz

c) Example dataset of images at 300 GHz

Fig. 15 shows some simulated snapshots of a dataset of ISAR images at 300 GHz of the Calipso satellite, based on the use cases considered on section II.B, which predict an aspect angle varying between 0°-90° with only slight change orientation of the OS wrt the MS.

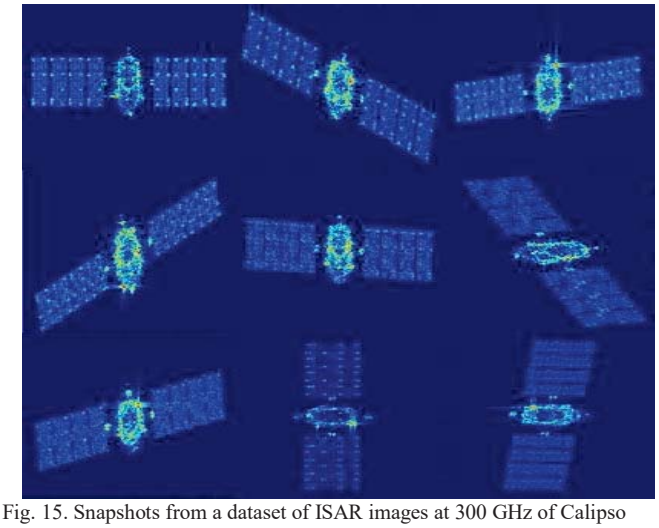

Fig. 15. Snapshots from a dataset of ISAR images at 300 GHz of Calipso

V. CONCLUSIONS

In this paper a use case and feasibility study has been presented to demonstrate the concept of ISAR imagery of space objects from a sub-THz sensor positioned on a satellite.

A. Application scenario.

The asserted scenario is that sensor will be steered onto the object to be imaged using ephemeris data on the target which

would be provided by other sensors, for example the global network of ground-based SSA radars. A unique feature of this system, compared to ground-based observations, is, of course, its ability to image aspects of the objects which are not visible from the earth.

The envisaged system therefore will be able to provide imaging data which will supplement that which can be obtained from ground-based sensors. It can be seen that the concept will remain viable for any orbital arrangement where the relative velocities of the satellites are of the same order as for the case explored in section II, and where the satellites are relatively tightly clustered in altitude, i. e. with the ± 100 km range of the sensor. The chosen altitude and detection range close to clusters of orbits ranging from LEO to GEO allow the system to survey a large number of other satellites. A small number of observation satellites would thus be able to image a large number of objects in orbit. If the targets are spread more widely in altitude other orbital designs can be considered, trading between the number of monitoring satellites and the revisit time to image each potential target.

The power budget has been analyzed to show that we can expect to be able to image relatively small satellites at 100 km range. This would require a significant stretch of current research into vacuum tube transmitters at these frequencies, but the 'stretch' required is not unreasonable.

B. Cross Range Resolution

The cross-range resolution obtained from a staring antenna will be of the order of 12 cm. It can be improved, down to perhaps 1 cm, if there is any internal rotation or wobbling of the target of which the processing can take advantage.

The resolution could also be improved by broadening the antenna in the direction of the target motion. The lower directivity will be compensated by the longer integration time, as the target will then be in the beam for longer, but the reduced received aperture must be compensated by making the antenna larger in the cross-track direction. This would lead to a complication in the mechanical design. Another possibility would, of course, be to steer the antenna to follow the course of the target, to increase the dwell time, but this would also increase the demands on the turning gear. This method of increasing the dwell time would also increase the noise-limited sensitivity of the system.

The decision as to whether to implement any improved resolution, and perhaps sensitivity, should be made following a cost-benefit analysis which would have to consider both the operational benefits which the improvements would give in the scenarios where the system will actually be used and also the through-life costs associated with the improvements. The costs include not only the cost of building more sophisticated turning gear, but also, for example, the increased design and testing effort required for it, increased launch costs if the weight is increased and any increased demands on quality of the ephemeris data required to steer the antenna. A related aspect will be the more general study of how well future techniques of prediction of satellite ephemeris will be able to meet the antenna pointing accuracy requirements of the concept.

In the future electronic scanning may be available and cost-effective at Sub-THz frequencies, perhaps using novel scanning strategies suited to these short wavelengths [26].

C. Exploiting the Richness of the Data

The paper has also examined the image-formation algorithms which will be required for this application and has proposed simple electromagnetic modeling to simulate images which the system would form, in order to (i) demonstrate how these algorithms would work; (ii) to create a comprehensive dataset of images seen by the sensors at any orientation and aspect angles which can be used to train semantic classifiers. The simulated results have demonstrated the richness of the imagery which the proposed system would be able to deliver.

An obvious next step will be to look at how this richness can be used to support image analysis and classification, for example how the recognition of the images can be aided by the accurate ephemeris data available from the SSA.

D. Further Work

The work in this paper has established that the system will be viable and provide unique information about objects in earth orbit. There is obviously great scope for more work. As well as looking at the imaging/recognition discussed in the previous paragraph, there is also scope for trade-offs between sensor range, number of sensors, number of satellites which are observable and update time between opportunities to image a particular satellite. Another possible trade-off is between adding the ability to steer the antenna, to increase the dwell time and the corresponding reduction in the transmitter power needed.

APPENDIX I: Analysis of Ray Tracing Modelling of Rough SURFACES

This appendix analyses the applicability of the electromagnetic simulation technique which was used, dividing the surface into a number of small facets and then calculating the signal reflected from each facet, to rough surfaces.

If the facets are small there will have a reflection coefficient proportional to $\mathrm{sinc}(\pi d\theta/\lambda)$, where, of course, d is a measure of the size of the facet, θ, is the angle of incidence, λ is the wavelength and $sinc(x) = sin(x)/x$. This means that if a curved surface is modelled by facets such that the angle between adjacent facets is less than λ/d, there will always be one facet which has a significant reflectivity back towards the radar, so the surface can be modelled accurately.

The change in orientation between two small facets of size d when modelling a surface of radius r is approximately d/r so to model the surface accurately we must have

$$\lambda / d > d / r \tag{17}$$

or

$$d < \sqrt{\lambda r} \tag{18}$$

For example, if $d = 10\lambda$ then the representation will be adequate if $r > 100\lambda$. If the irregularities are assumed to be spherical with a height h then they must subtend an angular range $\pm \phi$ at the centre of the sphere such that

$$r\left[1-\cos\phi\right] = h \tag{19}$$

for small angles:

$$r\phi^2 / 2 \approx h \tag{20}$$

$$\phi = \sqrt{2h/r} \tag{21}$$

The width of the irregularities, i. e. their period, must be at least

$$l \approx 2r\sin\phi \approx 2r\phi = 2\sqrt{2hr} = 2\sqrt{2hd^2/\lambda} = 2d\sqrt{2h/\lambda} \tag{22}$$

For the modelling described in section IV.B, and shown in Fig. 8, h=0.8 mm, the sizes of the facets have been chosen to be $d = 10\lambda$, thus at 75 GHz we have d=40 mm and the minimum allowable period is about l=50 mm and at 300 GHz we have d=10 mm and l=25 mm. The minimum radii of the irregularities (r=100λ) are 400 mm and 100 mm respectively, so the small angle approximation is certainly quite valid at 300 GHz. Although the faceting appears crude to the eye at 75 GHz, we can see that it is fine enough to accurately model the roughness, i. e. the lower density of returns at 75 GHz is not due to rays failing to find a facet which reflects back to the radar.

APPENDIX II: Noise Equivalent RCS of distributed scatterers to be imaged

One of the potential benefits of Sub-THz imagery is that it will include distributed returns from most surfaces constituting a target, in addition to discrete scatterers, or bright scattering points, cluster of which corresponding to extended target is typically considered as an ISAR image of the target.

Indeed, at low frequencies during image synthesis there may be only a few scattering points with required SNR, which makes recognition of a target a difficult task. If, however more diffused scattering is provided by "rough surfaces", then ISAR imagery can be considered as a superposition of set of bright scatterers and "clutter map", leading to more complete image and, therefore, ability to reveal shape of the target and, importantly, it's sub-parts. This can be achieved by moving up in frequency, so that surfaces, smooth and not resolvable at lower frequencies, start to become "rough". Higher sensitivity of the wavelength of around 1 mm to the texture/roughness of the surface can be expressed in terms of the increase of Normalized RCS (σ°, dBm^2/m^2) [27] of clutter, which depends on frequency, surface type, grazing angle and polarization. The magnitude of surface clutter return is determined by σ^o and the size of the resolvable clutter patch, A_g, or resolution cell. The sensitivity of the conventional SAR system to "clutter" returns is defined in terms of the Noise Equivalent RCS (NERCS). NERCS is the value of σ° giving SNR≡1, defining the weakest return which will be above the thermal noise floor.

It is useful to adapt this method to characterize the sensitivity of proposed ISAR system to the distributed scatterers constituting the target.

Assuming fixed spot beam of 0.23°, and therefore, a relatively small change of grazing angle within the ISAR integration time we may for simplicity use SAR estimates to calculate NERCS of typical surfaces to prove that it will be resolved (imaged) by radar justifying the hypothesis of advantage of using sub-THz frequencies.

1) NERCS of clutter for SAR – main consideration.

Azimuth compression in SAR defines the cross-range resolution as distance between nulls of the *sinc* function defining the envelope of the azimuth compressed SAR data:

$$S_{out}(t) = e^{-j\gamma t^2}\cdot \mathrm{sinc}[\gamma T_{\mathrm{int}} t];$$
$$\mathrm{sinc}[\gamma T_{\mathrm{int}} t] = \mathrm{sinc}\left[\frac{T_{\mathrm{int}}\, 2\pi v^2}{\lambda R} t\right] \tag{23}$$

where $\gamma = 2\pi v^2/(\lambda R)$ corresponds to a phase of the received signal, R and v are the slant range and along-track velocity of the platform, respectively, and T_{int} is the integration time.

First two nulls at $t_{nulls} = \pm\lambda R/(T_{\mathrm{int}} 2v^2)$ define cross range resolution as half the distance between nulls, Δt :

$$\Delta X = \Delta t \cdot v = \frac{\lambda R}{2T_{\mathrm{int}} v} = \frac{\lambda R}{2D_{SA}} \overset{D_{SA}=\frac{\lambda R}{d}}{=} \frac{d}{2} \tag{24}$$

where full aperture size D_{SA} defines full aperture synthesis time $t_A = \lambda R/(2\Delta X \cdot v)$, d is the physical aperture.

SAR processing is essentially a matched filtering, so that

$$\mathrm{SNR} = \frac{E}{k\cdot T_s} \tag{25}$$

The energy of the signal

$$E = P_{R,av}\cdot t_A = \frac{P_{T,av}G^2\lambda^2\sigma}{(4\pi)^3 R^4}\cdot t_A = \frac{P_{T,av}G^2\lambda^2}{(4\pi)^3 R^4}\sigma^0 A_g \cdot t_A \tag{26}$$

where $P_{T,av}$ is the average transmit power and, A_g (a resolvable "clutter patch" area) is, in fact an area of the SAR pixel and equals to $\Delta X\cdot\Delta R/\cos\psi$, where ψ is the grazing angle (equal to aspect angle α in Section II). Therefore substituting values for A_g and t_A in (25) we can express CNR as

$$\mathrm{SNR} \overset{(\Leftrightarrow CNR)}{=} \frac{P_{T,av}G^2\lambda^3}{(4\pi)^3 R^3}\frac{\sigma^0\Delta R}{2\cos\psi\cdot vkT_s} \tag{27}$$

The noise equivalent normalized cross section, NERCS, which can be used to assess if the clutter (in our case - returns from satellite surfaces) can be resolved is therefore:

$$NE\sigma^0 = \frac{2(4\pi)^3 R^3\cos\psi\cdot v\cdot kT_s}{P_{T,av}G^2\lambda^3\Delta R} \tag{28}$$

where the condition CNR=1 is used. If σ^o is larger than NERCS we can expect return to be above the noise floor of the system.

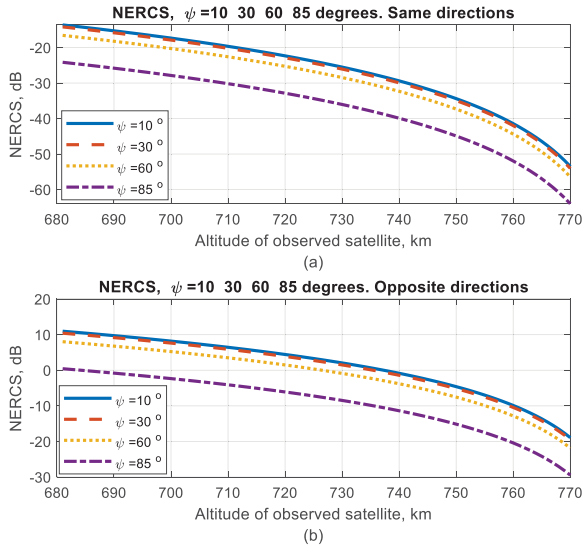

Fig. A.1 Illustrative example $NE\sigma^o$ vs R_o, for four grazing angles, R_m=780 km; (a) same direction of MS and OS; (b) opposite directions.

Illustrative example: Given parameters defined in Sections II and III.A for LEO use case: P_{avg}=20 W, G=57 dB, f=300 GHz, B=20 GHz, T_s=1200 K, plots of NERCS vs altitude of the OS are shown for 4 grazing angles in Fig. A.1.

Two main conclusions can be drawn here: (1) surface facets of OS oriented at grazing angles w.r.t radar will be less resolved, than that at close to perpendicular incidence; (2) higher relative velocity is less favorable.

2) Transition from specular to diffused scattering with increase of frequency.

Such transition relates to the fact, that surface changes from being "smooth" to "rough" w.r.t wavelength, providing higher backscattering when frequency increases. The illustration of results of measurements of σ^o for surfaces of different roughness are shown in Fig A.2 at two frequencies 79 GHz and 150 GHz from [8]. Different roughness was provided by sandpaper of different grit with calibrated average size of the particles. Backscattering coefficient at 150 GHz (b) is increased for the roughest sample of grit 40 at grazing angles (or high incidence angles of axes in Fig.A.2) by 15 dB, indicating the fact that the 2 mm wavelength is comparable with the physical roughness of this surface. It was shown in [8], that with further increase of frequency specular scattering mechanism gradually change to diffused for all samples so that σ^o of the surface increases. Considering the values of σ^o in the range [2-10] dB for the grazing angles from 85° to 90° and drops to -17 dB at 60 degrees and comparing with results of NERCS in Fig. A.1 (b) we can conclude that proposed ISAR radar will be best suited to image small features/surfaces of observed object at aspect angles ~85°, which suits well the scenario of the narrowbeam antenna looking down to the object in the case of opposite motion of satellites at longest distance of 100 km (See Fig. 3 (b)), other angles closer to grazing angles are expected for shorter ranges, in which cases NERCS is smaller. On the other hand considering longer integration time than extreme values obtained for the same orbital plane of oppositely moving satellites, we can expect to be able to resolve return from surfaces at nearly all anticipated grazing angles.

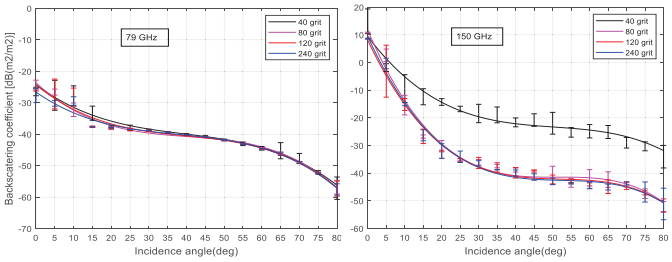

(a) (b)

Fig. A.2. Results of measurements in [8] of the NERCS (σ^o_{vv}) of sand paper of different roughness (grit 40 (mean particle size 0.34 mm, roughest), to 240 (mean particle size 0.07 mm -very smooth)): (a) 79 GHz and (b) 150 GHz .

ACKNOWLEDGEMENT

This work is sponsored by the Defense Science and Technology Laboratory (DSTL), United Kingdom, as part of the Defense and Security Accelerator (DASA) competition, contract number: DSTLX1000141364.

REFERENCES

[1] Lal, B., et al., "Global Trends in Space Situational Awareness (SSA) and Space Traffic Management (STM)," IDA Science & Technology Policy Institute, Washington, DC, USA, IDA Document D-9074 Log: H 18-000179, 2018
[2] Console, A. "Command and Control of a Multinational Space Surveillance and Tracking Network", Joint Air Power Competence Centre, Germany, 2019
[3] Ender, J., et al., "Radar techniques for space situational awareness," 12th Int. Rad. Sym. (IRS), Leipzig, 2011, pp. 21-26
[4] Pillai, S.U., et al., Space Based Radar: Theory & Applications, McGraw Hill, New York, 2008, pp. 77–97
[5] Benson, C. R., "Enhancing space situational awareness using passive radar from space based emitters of opportunity," 2014 Mil. Com. and Inf. Sys. Conf. (MilCIS), Canberra, ACT, 2014, pp. 1-5
[6] Chen, V. C. and Martorella, M., "Inverse Synthetic Aperture Radar Imaging: Principle, Algorithm, and Applications". Edison, NJ, USA: SciTech, 2014, pp. 77-94
[7] Sabery, S. M., et al., "Surface Classification Based on Low Terahertz Radar Imaging and Deep Neural Network," 21st Int. Rad. Sym. (IRS), Warsaw, Poland, 2020, pp. 24-27
[8] Sabery, S. M., et al., "Study of Low Terahertz Radar Signal Backscattering for Surface Identification". Sensors 2021, 21, 2954.
[9] N2YO - LIVE REAL TIME SATELLITE TRACKING AND PREDICTIONS. https://www.n2yo.com/
[10] Daniel, L., et al., "Application of Doppler beam sharpening for azimuth refinement in prospective low-THz automotive radars," in IET Radar, Sonar Navigation, vol. 12, no. 10, 2018, pp. 1121-1130
[11] Ploskin, A. E., et al., "Performance improvement of a sub-THz traveling-wave tube by using an electron optic system with a converging sheet electron beam," Results in Physics, Volume 12, 2019, Pp. 799-803
[12] Tessmann, A., et al., "A 300 GHz low-noise amplifier S-MMIC for use in next-generation imaging and communication applications," 2017 IEEE MTT-S International Microwave Symposium (IMS), 2017, pp. 760-763
[13] Stove, A. G., "Linear FMCW Radar Techniques," n IEE Proceedings F, Radar and Signal Process., vol. 139, no. 5, 1992, pp. 343-350
[14] Stove, A. G., "Erratum to 'Linear FMCW Radar Techniques," IEE Proc F, Radars Signal Process. , vol. 140, no. 2 1992, pp. 137
[15] Hamilton, S., " F. M. and A. M. Noise in Microwave Oscillators," Microwave J., 1978, pp 105-109.
[16] 2LPL Series Phase-Locked Oscillator – L3Harris Data Sheet, 2019
[17] Daryoush, A. S., et al., "Optoelectronic Oscillators: Recent and Emerging Trends," Microwave Journal, 2018, pp. 58–76
[18] Zhu, D., et al., "Robust ISAR Range Alignment via Minimizing the Entropy of the Average Range Profile," in IEEE Geoscience and Remote Sensing Letters, vol. 6, no. 2, 2009, pp. 204-208
[19] Özdemir, C., "Inverse Synthetic Aperture Radar Imaging With MATLAB Algorithms." Hoboken, NJ, USA: Wiley, 2012, pp. 274-283
[20] Marchetti, E., et al., "Space-borne Sub-THz ISAR System for Objects with Translational Motion," 2020 IEEE Radar Conference (RadarConf20), Florence, Italy, 2020, pp. 1-6
[21] García-Fernández, A. F., et al., "Facet Model of Moving Targets for ISAR Imaging and Radar Back-Scattering Simulation," in IEEE Transaction on Aerospace and Electronic Systems, vol. 46, no. 3, 2010, pp. 1455-1467
[22] Cendes, Z., et al., "Magnetic field computation using Delaunay triangulation and complementary finite element methods," in IEEE Transactions on Magnetics, vol. 19, no. 6, 1983, pp. 2551-2554
[23] Möller, T., and Trumbore, B., "Fast, minimum storage ray-triangle intersection." Journal of graphics tools 2.1, 1997.
[24] Mahafza, B. R., "Radar systems analysis and design using MATLAB", CRC press, 2002.
[25] 3D Models - NASA 3D Resources, https://nasa3d.arc.nasa.gov/models
[26] International Patent Application No. 1803922.2, 'Phased Array Antenna Device,' Filed 12th March 2019.
[27] Richards, M., "Fundamentals of Radar Signal Processing. US: McGraw-Hill Professional, 2005, Chapter 2

Emidio Marchetti received the M.Eng. degree in communication engineering from 'La Sapienza' University of Rome, Italy, the M.Sc degree in RF and microwave engineering and the Ph.D. in radar systems from the University of Birmingham, UK. He is Research Fellow at the Microwave Integrated Systems Laboratory, UoB. His research interests include automotive radar systems, THz sensing, ISAR imaging, spaceborne radar systems.

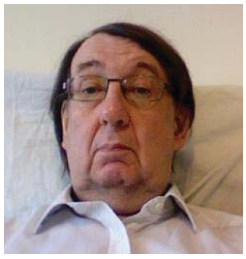

Andrew G. Stove (M '98–SM '04) obtained a BA is Engineering Science in 1977 and a D. Phil for work on surface acoustic wave devices in 1981, both from Oxford University.
In 1980 he joined Philips Research Laboratories in Redhill, England, where he worked on FMCW radar systems with applications in smart ammunition, automotive radar and low probability of intercept marine navigation. In 1996 he joined Racal Radar Defence Systems, which is now part of Thales, where he worked on the design for the Searchwater 2000 radar family, and on the analysis of the subsequent trials data, including improving the understanding of the behavior of the sea clutter. In 2015 he left Thales and he now works at the University of Birmingham.
Dr. Stove is an honorary professor at the University of Birmingham and a visiting professor at UCL and is also a Fellow of the Institution of Engineering and Technology (the successor of the Institution of Electrical Engineers).

Edward G. Hoare (SM'99) received the Ph.D. degree in over-the-horizon radar from the School of Electronic and Electrical Engineering, University of Birmingham, following an apprenticeship at The Royal Radar Establishment, College of Electronics, Malvern, U.K. and a spell in industry. Over the past 20 years, he has provided sensor, antenna, and millimetre-wave radar consultancy to Jaguar Cars, Land Rover, and The Ford Motor Company, delivering over 60 technical reports on millimeter-wave antennas, radar, signal processing, sensors and associated topics. He holds a number of patents in automotive radar and sensors. His research interests include radar systems and antennas covering frequencies from 2 MHz to over 1 THz, including non-cooperative bistatic radar, forward scatter maritime radar, radar acoustic sounding, millimeter-wave automotive radar, and Low-Terahertz radar. He is currently a Senior Research Fellow with the Microwave Integrated Systems Laboratory, University of Birmingham and was a member of the European Automotive Radar Standards Group.

Mikhail Cherniakov received the Ph.D. and D.Sc. degrees from the Bauman Moscow Technical University, Moscow, Russia, in 1980 and 1992, respectively.
He was the Chair in Aerospace and Electronic Systems with UoB. He has 45 years of experience in radar Research and Development. Starting his carrier at Moscow Technical University (MIET), Moscow, Russia, he was the Founded Head of the Radar Laboratory with nearly 50 full-time Research Staff. In 1994, he was a Visiting Professor with the University of Cambridge, Cambridge, U.K., and from 1995 to 2000, he was with The University of Queensland, Brisbane, QLD, Australia. During this period, he co-founded GroundProbe Ltd., Brisbane, which is now the biggest radar company in Australia with multiple divisions around the world. In 2000, he joined the UoB, where he founded the Microwave Integrated Systems Laboratory (MISL) with about 25 researchers working now in various areas of radar and remote sensing. He is the author of more than 300 publications and an editor/author of three books.
Dr. Cherniakov was the first scientist awarded the Christian Hülsmeyer Prize for his activity in radar Research and Development in 2017. From 2016 to 2019, he was the Founded Chair of the Electromagnetic Systems Interest Group (EMSIG)—The UK Radar Society.

David Blacknell holds a B.A. in Mathematics from Cambridge University, an M.Sc. from University College London, a Ph.D. from Sheffield University and is a Fellow of the Institute of Physics. He worked at the GEC-Marconi Research Centre from 1984 to 1991 and at QinetiQ (formerly DERA) from 1991 to 2007 where he was awarded a QinetiQ Fellowship in 2002. He took up the Chair in Radar Systems at Cranfield University in April 2007 and was Head of the Radar Group until December 2008. He currently works at DSTL, where he became a Dstl Fellow in October 2011, and is a visiting Professor at University College London. He has worked on a large variety of topics in radar signal and image processing during his career and has published extensively.

Marina Gashinova received the M.Sc. degree in mathematics from Saint Petersburg State University, Saint Petersburg, Russia, in 1991, and the Ph.D. degree in physics and mathematics from Saint Petersburg Electrotechnical University, Saint Petersburg, in 2003. In 2006, she joined the Microwave Integrated System Laboratory, University of Birmingham, Birmingham, U.K., where she is the Chair of Pervasive Sensing, the Head of the Pervasive Sensing Group, and leading a number of research projects on automotive sensing and terahertz sensing.